Title

Pairing of Aqueous and Nonaqueous Electrosynthetic Reactions Enabled by a Redox Reservoir Electrode.

Journal

Journal of the American Chemical Society, 144(49)

Authors

Michael, Katelyn
Su, Zhi-Ming
Wang, Rui
et al.

Publication Date

2022-12-14

DOI

10.1021/jacs.2c09632

Peer reviewed

Published in final edited form as:

J Am Chem Soc. 2022 December 14; 144(49): 22641–22650. doi:10.1021/jacs.2c09632.

Pairing of Aqueous and Non-Aqueous Electrosynthetic Reactions Enabled by a Redox Reservoir Electrode

Katelyn H. Michael[1], **Zhi-Ming Su**[1], **Rui Wang**[1], **Hongyuan Sheng**[1], **Wenjie Li**[1], **Fengmei Wang**[1,2], **Shannon S. Stahl**[1], **Song Jin**[1]

[1]Department of Chemistry, University of Wisconsin-Madison, 1101 University Avenue, Madison, Wisconsin 53706, USA.

[2]State Key Laboratory of Chemical Resource Engineering, College of Chemistry, Beijing University of Chemical Technology, Beijing, 100029, China

Abstract

Paired electrolysis methods are appealing for chemical synthesis because they generate valuable products at both electrodes; however, development of such reactions is complicated by the need for both half-reactions to proceed under mutually compatible conditions. Here, a modular electrochemical synthesis (ModES) strategy bypasses these constraints using a “redox reservoir” (RR) to pair electrochemical half-reactions across aqueous and non-aqueous solvents. Electrochemical oxidation reactions in organic solvents, the conversion of 4-*tert*-butyltoluene to benzylic dimethyl acetal and aldehyde in methanol or the oxidative C–H amination of naphthalene in acetonitrile, and the reduction of oxygen to hydrogen peroxide in water were paired using nickel hexacyanoferrate as a RR that can selectively store and release protons (and electrons) while serving as the counter electrode for these reactions. Selective proton transport through the RR is optimized and confirmed to enable the ion balance, and thus the successful pairing, between redox half-reactions that proceed with different rates, on different scales, and in different solvents (methanol, acetonitrile, and water).

Graphical Abstract:

Corresponding Authors: Song Jin; jin@chem.wisc.edu, Shannon Stahl; stahl@chem.wisc.edu.

The authors declare no competing financial interest.

Supporting Information

The Supporting information is available free of charge at

Experimental methods, additional figures and tables on materials characterization, electrochemical measurements, and NMR spectra of the reaction products.

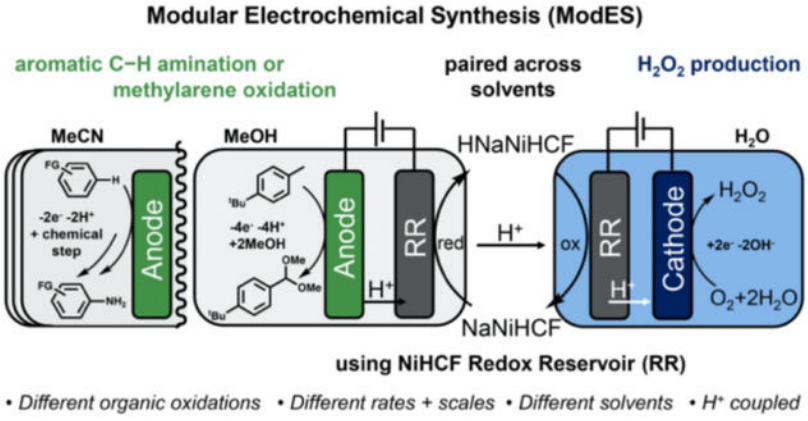

Introduction

Electrochemical synthesis is the focus of increased attention, owing to its ability to avoid elevated temperatures, pressures, eliminate stoichiometric chemical reagents, and reduce chemical waste.[1–6] In typical electrosynthetic reactions, the desired chemical transformation taking place at the working electrode is balanced by a sacrificial reaction that takes place at the counter/auxiliary electrode. Anodic oxidations, such as conversion of a primary alcohol to a carboxylic acid,[7] are typically balanced by proton reduction to hydrogen gas at the cathode. Cathodic reductions, such as the dimerization of acrylonitrile to adiponitrile,[8] are often balanced by water oxidation to O_2 at the anode. Smaller scale electrosynthetic reductions commonly use a sacrificial metal anode, such as Zn or Fe. The non-productive counter electrode reactions are designed to balance the charge and avoid interference with the reaction of interest; however, it would be ideal if the non-productive reaction at the counter electrode could be replaced with a redox reaction that generates a valuable product.[9–11] Such “paired electrolysis” methods can improve the efficiency, sustainability, and/or economics of large scale applications.[6,9–16] A prominent example of paired electrolysis developed by BASF features the oxidation of 4-*t*-butyltoluene and the reduction of dimethyl-*o*-phthalate in methanol solvent (Figure 1a).[5,17,18] The process is formally 100% atom efficient owing to its perfect methanol and electron balance. Both products may be formed at the same rate under the identical reaction conditions (temperature, solvent, supporting electrolyte, etc.) and rates. This matching of reaction conditions and rates presents a challenge to the development and widespread adoption of paired electrochemical reactions, as the optimal conditions and rates of different reactions are seldom identical.[6,11,19]

The challenges for achieving paired electrolyses can be alleviated by recently described redox reservoir (RR) enabled modular electrochemical synthesis (ModES) methods.[20] RRs are solid-state battery materials that temporarily store/release ions and electrons to balance the ion/electron transfer steps taking place at the working electrode. Therefore, RRs can serve as a universal counter electrode, capable of pairing alternately with both cathodic and anodic half-reactions. Implementation of this RR-based ModES concept relaxes the constraints of paired electrochemical synthesis because the paired half-reactions may be

carried out in different cells, and at different times, locations, rates, and/or scales, to align with demand. The promises of the ModES strategy have been demonstrated by the reports on decoupled water splitting, which can reduce the crossover of oxygen impurity in the produced hydrogen and provide a means to reduce gas purification costs and safety hazards.[21–27] Moreover, RRs can enable the pairing of many incompatible half-reactions to synthesize value-added chemicals such as the co-production of several high value oxidants in aqueous media using an RR,[20,28] which was not previously possible due to product and membrane compatibility. RRs could also enable electrosynthetic reactions to take place in an undivided cell instead of the commonly used divided cells, bypassing the need for a membrane or separator. To date, the ModES strategy has only been used to pair two redox half-reactions in aqueous solutions, but it should be compatible with non-aqueous solvents commonly used in organic electrosynthesis.[3,6,10,28]

To expand the flexibility and potential utility of ModES, we elected to investigate the use of a solid-state RR to pair two electrosynthetic redox reactions conducted in different solvents. These half-reactions include the methylarene oxidation reaction featured in the BASF process, conducted in methanol at the anode (Eq. 1 and Figure 1a), and electrochemical hydrogen peroxide production via two-electron reduction of O_2 in water at the cathode (Eq. 2 and Figure 1b).

$$4-tBuC_6H_4CH_3 + 2\,CH_3OH \rightarrow 4-tBuC_6H_4CH(OCH_3)_2 + 4\,H^+ + 4e^- \quad \text{(Eq. 1)}$$

$$O_2 + 2\,H_2O + 2e^- \rightarrow H_2O_2 + 2\,OH^- \quad \text{(Eq. 2)}$$

These important reactions are performed on very different scales industrially, 10^3 and 10^6 tons per year for methylarene oxidation and H_2O_2 production, respectively. Electrochemical production of H_2O_2 for disinfection, environmental applications, or as an oxidant for chemical synthesis is the focus of growing interest as an alternative for the traditional chemical anthraquinone process that requires high energy consumption, expensive catalysts, and multiple steps.[29–32] The susceptibility of H_2O_2 to decomposition limits compatible half-reactions therefore the H_2O_2 electrolyzer usually has the oxygen evolution reaction (OER) as the anodic process separated by an expensive ion exchange membrane (Figure 1b). The use of RRs in a ModES strategy could eliminate the unproductive counter reactions and the need for ion exchange membranes, but RR electrodes that can transfer the common ions that are involved in both half-reactions need to be developed to maintain the ion-balance and realize sustained co-production of chemicals.[33,34]

Here, we demonstrate the pairing of these two half-reactions across aqueous and non-aqueous solvents using a carefully designed RR that results in the following overall ModES reaction (Figure 1c):

$$2\,O_2 + 4-tBuC_6H_4CH_3 + 2\,CH_3OH \rightarrow 2\,H_2O_2 + 4-tBuC_6H_4CH(OCH_3)_2 \quad \text{(Eq. 3)}$$

The anodic methylarene oxidation reaction generates H^+ in the undivided cell and the RR undergoes reduction with H^+ intercalation (Figure 1c, left). Then, the RR electrode is transferred to a separate undivided cell where it supports cathodic hydrogen peroxide production by undergoing oxidation and release of H^+ (Figure 1c, right), which neutralizes the OH^- produced by H_2O_2 production (Eq. 2, 4).

$$O_2 + 2\ H_2O + 2H^+ + 2\ e^- \rightarrow H_2O_2 + 2\ H_2O \quad \text{(Eq. 4)}$$

The overall process avoids contact between the supporting electrolytes of the two half-reactions, while allowing for ion balance between two incompatible processes. We identify a Prussian blue analogue material, nickel hexacyanoferrate (NiHCF), that is compatible with both aqueous and non-aqueous solvents as the RR to ensure selective transport of protons across the electrochemical cells. After optimization of the RR material, reaction electrolytes, and ModES process, continuous proton-balanced ModES cycles with pH stability that yield complete conversion of methylarene in methanol and the production of H_2O_2 in water are achieved. To further support the flexibility of the ModES strategy, the amination of naphthalene in acetonitrile is paired with H_2O_2 production using the same NiHCF RR.

Results and Discussion

Synthesis and electrochemical performance of NiHCF as a redox reservoir

The RR materials for the ModES processes should be selected based on their ability to transport the balancing ion, chemical and electrochemical stability in the appropriate electrolytes, their redox potential, cycling capacity, and kinetics. For the ModES pairing herein, proton is the balancing ion, therefore we selected Prussian blue analogues (PBAs) because they have been reported as proton battery materials.[35–37] The rigid open framework and large interstitial sites with a three-dimensional diffusion channel along the <110> crystallographic directions in PBAs make them advantageous for intercalation of ions in aqueous and non-aqueous solution.[37,38] PBAs are also inexpensive and can be synthesized at scale using a simple co-precipitation method. Various PBAs, including NiHCF and CuHCF, were tested for stability in a range of solvents commonly used in batteries and organic electrochemical reactions. First, a small amount of PBA powder was added to the solvents to check for solubility. If there was no visible dissolution, a cyclic voltammogram (CV) was taken to find the formal potential of the PBA followed by cycling tests. NiHCF was found to be the most stable PBA in nonaqueous solvents and undergoes redox in methanol, DMF, and acetonitrile (Figure S1).

We synthesized the rhombohedral NiHCF crystals with occupied Na^+ following a reported co-precipitation method.[39] Scanning electron microscopy (SEM) images of the as-synthesized crystals show well-faceted microcubes with an average size of approximately 2 μm (Figure 2a inset). Powder X-ray diffraction (PXRD) pattern displays the characteristic doublet diffraction peaks of the rhombohedral phase at (220), (440), and (660) compared to the standard pattern that represents the cubic phase (JCPDS no. 52–1907) (Figure S2). The as-synthesized rhombohedral phase is preferred due to its slightly higher capacity compared to the cubic (oxidized) phase and its larger unit cell.[40] Inductively coupled

plasma optical emission spectroscopy (ICP-OES, Table S1) and thermogravimetry analysis (TGA, Figure S3) were conducted to determine the compositions of Na, Ni, Fe elements and the water content in the NaNiHCF sample to confirm the exact formula to be $Na_{2.29}Ni[Fe(CN)_6]_{1.04}{\cdot}2.2\ H_2O$.

We then studied the electrochemical behaviors of the NiHCF electrode intercalating and de-intercalating proton in both methanol and aqueous solutions using a three-electrode set up. The as-synthesized NiHCF was always oxidized before use to allow for intercalation of proton upon reduction. When NiHCF (cubic phase) is reduced with the intercalation of proton rather than an alkali metal cation, the crystal structure remains cubic and does not shift to rhombohedral (Figure S4–5). Before all electrochemical tests, the NiHCF electrode was reduced and oxidized 10 times (Figure S6) to activate the electrode. The charge/discharge rate of 1 C (meaning the material is fully discharged in one hour, and a rate of n C means the battery is fully discharged in 60/n minutes) was determined based on the capacity of NiHCF in neutral aqueous solutions (65 mAh g^{-1}). The stability tests show that NiHCF can be cycled repeatedly using proton in methanol with only 1% decay over 50 cycles (Figure 2a) and in water with a 9.76% decay after 50 cycles (Figure 2d). Cyclic voltammograms (CVs) of NiHCF at different scan rates show reversible redox behavior with a NiHCF working and counter electrode in an undivided cell (Figure 2b, 2e), following this reaction:

$$NaNi\left(Fe^{3+}(CN)_6\right) + H^+ + e^- \rightleftarrows HNaNi(Fe^{2+}(CN)_6) \quad \text{(Eq. 5)}$$

With proton intercalation it is common to see multiple CV peaks, which is usually attributed to the binding of protons with ligand and zeolitic water molecules.[41,42] The potential window in acidic aqueous solution is −0.3 V to 1.0 V vs. SCE and NiHCF has a formal potential of 0.5 V (Figure 2e). In methanol, the potential window is −0.9 V to 1.1 V vs. Fc/Fc^+ with a NiHCF counter electrode (Figure 2b).

With the desired half reactions in mind, the RR stability bounds were tested. Hydrogen peroxide production can occur over a wide pH range, so the redox performance of the RR electrode was studied under different pH conditions. NiHCF was found to be stable to reduction in acidic to neutral conditions, but unstable in alkaline solution (Figure S7). However, NiHCF was stable to oxidation in weakly alkaline solution. Therefore, we could select an aqueous H_2O_2 production supporting electrolyte with a pH from 0 to 11, in which oxidation of NiHCF will take place. For the cell in which NiHCF reduction takes place, the aqueous supporting electrolytes could be acidic to neutral. When undergoing reduction in methanol, NiHCF had more severe dissolution. It was reported that excess Ni ions in solution help stabilize the Prussian Blue structure, preventing Ni dissolution that results in leaching of the redox active Fe from NiHCF.[43] Therefore, we added 20 mM $NiNO_3$ into the methanol solution, which improved the cycling performance. Clear improvement of lattice stability is evident by the lack of precipitate formation after 50 cycles of reduction and oxidation in methanol solution and 23 cycles of ModES (Figure S9–10). Due to potential decomposition of H_2O_2 in the presence of nickel ions, Ni ions were not added in the aqueous electrolyte, but no color change or precipitate was observed when running H_2O_2 production.

NiHCF has worse rate capabilities in methanol than aqueous solutions presumably due to the reduced hydrogen bonding network.[44] After studying different cycling currents, keeping the C rate as low as possible during cycling in methanol proved to be essential for maintaining the capacity of NiHCF. A discharging rate not exceeding 1 C was selected for this half-reaction (Figure S8). In aqueous solutions, the rate capabilities are improved by stronger intermolecular forces as well as higher solution conductivity compared to organic solvents.[20] This means that aqueous half-reactions can be run at a higher rate than the non-aqueous half-reactions. A representative galvanostatic discharge curve of NiHCF (reduction) in methanol from 100% to 25% state-of-charge (SOC) is shown in Figure 2c. The corresponding galvanostatic charge curve (oxidation) in pH 11 aqueous solution is shown in Figure 2f.

Optimization of half-reactions

Literature precedents for the organic half reaction, methylarene oxidation reaction, provide an important foundation for the work conducted here.[18,45] Cyclic voltammograms, obtained in acetonitrile solvent, highlight a comparison of redox potentials associated with 4-*t*-butyltoluene and its corresponding intermediate and product relative to that of MeOH (Figure 3a). The plots show that the methylarene reagent and methyl ether intermediate undergo oxidation at potentials below that of methanol, while the product dimethylacetal is oxidized at a potential higher than that of methanol.

By adapting the previously reported conditions, direct oxidation of 4-*t*-butyltoluene delivered 68% yield of the corresponding dimethyl acetal in an undivided cell using graphite for both the working and auxiliary electrode (Figure 3b, entry 1). The reaction was conducted at a constant current of 20 mA, and the optimal yield was obtained after passing 8 F/mol of charge. The reaction did not reach completion when the theoretical charge of 4 F/mol was passed (40% product yield with 36% unreacted starting material, entry 2). A modest drop in yield was observed when more charge was passed (56% yield at 10 F/mol, entry 3), and decreased yields were also observed at lower and higher current densities (entries 4 and 5). $TBAPF_6$ was not as effective a supporting electrolyte as $TBAClO_4$ (entry 6). In anticipation of pairing methylarene oxidation reaction with a proton-exchange RR, a small amount of water was added to the methanol to facilitate proton transport within the RR. This modification resulted in partial hydrolysis of the dimethyl acetal, but a comparable overall acetal/aldehyde yield was obtained (64%, entry 7). The influence of added $Ni(NO_3)_2$ was tested to account for the stabilizing effect of Ni^{2+} ions on the stability of the NiHCF RR in methanol. The presence of 20 mM $Ni(NO_3)_2$ in the electrolyte had minimal impact on the reaction yield (65% yield, entry 8, Figure S11). On the other hand, control experiments confirmed that moderate quantities of Brønsted acid in solution (10 and 50 mol% with respect to the substrate) had a deleterious effect on the reaction, lowering the yield to 58% and 30%, respectively (entries 9 and 10).

For H_2O_2 production at the cathode, we used carbon based catalysts as the working electrodes due to their stability and good performance in neutral to alkaline conditions and their low cost.[46] Following previous reports, annealed carbon felt[20,29,47] and iron decorated carbon nanotubes[48] (10 nm width) (Fe-CNT, Figure S12) were prepared and tested in neutral

to weakly alkaline solutions (Figure S13–S15) with linear sweep voltammetry (LSV) in a divided cell with a Pt counter electrode to measure current density (Figure 3c). We chose a solution of 1.7 M Na_2SO_4 solution adjusted to pH 11 with 1 M NaOH for performing H_2O_2 electrosynthesis due to the high activity of H_2O_2 production, reduced competition with OER, and the stability of the RR. Under these conditions, the 2 cm^2 Fe-CNT cathode shows a current of −100 mA at 0.16 V vs. RHE (Figure 3c). Various applied potentials were screened using chronoamperometry (Figure S16) and the produced H_2O_2 was quantified chemically using titration (see details in the Supporting Information, Figure S17). The best current density and Faradaic efficiency (FE) was achieved using Fe-CNT electrodes on hydrophobic carbon fiber paper, similar to what was previously reported.[48] A potential of 0.244 V vs RHE was selected to ensure a high FE above 90% when accumulating 200 ppm of H_2O_2 in a 30 mL cell.

Proton balancing ability of the RR

The overall ModES reaction requires protons to be transferred from the methylarene oxidation reaction cell in methanol to the cathodic H_2O_2 production cell in water by the RR (Figure 1c). Therefore, it is important to study the ability of the RR electrode to transfer and balance protons. Protons have a smaller mass and ionic radius compared to metal ions and exhibit the fastest diffusion kinetics via the Grotthuss mechanism which allows protons to be transferred via a hydrogen bonding network (Figure 4a).[35,49] Under the Grotthuss proton conduction mechanism, zeolitic water in the PBA cages and ligand water in anion vacancies can form a continuous hydrogen bonding network that allows for concerted cleavage and formation of O-H bonds for proton transfer.[36]

In the beginning of the methylarene oxidation reaction process, there is a large excess of the supporting electrolyte cation and an absence of protons in solution. If a metal cation that can be intercalated into NiHCF, such as sodium, is present, it will compete with proton and result in ion imbalance. Unlike conventional batteries in which there is a large excess of the ions causing the redox, this ModES system requires the protons produced during anodic oxidation to be intercalated into the RR electrode. Because the reaction yield of the methylarene oxidation reaction is affected by high proton concentration (Figure 3b, entries 9 and 10), an acidic electrolyte cannot be used to alleviate ion competition. To manage this competition, we selected a tetrabutylammonium (TBA) cation based supporting electrolyte, $TBAClO_4$, to ensure preferred intercalation of protons based on cation size (Figure 4a). TBA^+ has an approximate diameter of 9.9 Angstroms,[50] which is larger than that of the NiHCF cage (5.1 Å),[51] thus ensuring exclusion from the cage. In contrast, the desolvated ionic diameter of Na^+ is 1.9 Å, allowing it to compete with protons.[52]

To further improve the proton uptake into the RR, we also varied the water-to-methanol ratio as the solvent for the methylarene oxidation reaction. The addition of water enhances the kinetics of proton intercalation by improving the hydrogen bonding network and improves the solution conductivity compared to a purely methanol solution.[53] Even though adding water introduces competition between OER and the methylarene oxidation reaction, the benefits of improved conductivity and kinetics outweigh the slight loss in FE and minimal decrease in product yield (cf. Figure 3b). We found that the optimal water-to-methanol

ratio is 1:20, which retained the methylarene oxidation reaction product yield and Faradaic efficiency while improving RR performance.

To evaluate the proton (de)intercalation by the NiHCF RR, we ran hydrogen peroxide production in undivided and divided cells to monitor pH changes with the RR as the counter electrode. In the divided cell there is a glass frit dividing the working and counter electrode chambers to slow down ion movement, primarily allowing the supporting electrolyte ions to pass between the two chambers to maintain charge balance. As a result, pH shifts can be measured in the two chambers immediately following the electrochemical experiment. The RR was first reduced in methanol with 1 M H_2SO_4 as the supporting electrolyte. For the RR oxidation, the supporting electrolyte was a 1.7 M Na_2SO_4 and 1 mM NaOH aqueous solution. In the divided cell, an increase of 1.91 pH units was observed in the working electrode compartment due to the hydroxide released during H_2O_2 production (Figure 4b, red trace). In the counter electrode compartment, there was a decrease of 7 pH units from the protons deintercalated from the NiHCF RR (Figure 4b, blue trace). In an undivided cell, all ions can diffuse through the cell and the same supporting electrolytes were used for the RR reduction and oxidation. Only a small pH shift of 0.45 pH units was observed in the undivided cell (Figure 4b, grey trace) because the proton deintercalated from the NiHCF neutralizes the hydroxide produced from H_2O_2 production. This demonstrates that the NiHCF RR is capable of balancing the protons across solvents.

For further support that protons are the ions that are intercalated into the NiHCF RR, we conducted operando electrochemical quartz crystal microbalance (EQCM) measurements during CV tests (Figure 4c and d) to monitor the electrode mass change (see details in Supporting Information). In PBAs, cation (de)intercalation must be charge balancing the redox process.[54] The EQCM results (Figure 4c, red trace) show during reduction (protonation) the electrode experiences a frequency increase indicating a mass loss according to the Sauerbrey equation:[55]

$$\Delta f_S = -\frac{2 * f_0^2 * \Delta m * n}{(\mu_q \rho_q)^{\frac{1}{2}}} \quad \text{(Eq. 6)}$$

which simplifies to:

$$\Delta f = -C_f * \Delta m \quad \text{(Eq. 7)}$$

where ρ_q is the density of the quartz crystal (2.648 g/cm^3), μ_q is the shear modulus of quartz (2.947×10^{11} g/cm*s^2), f_0 is the resonant frequency of the fundamental mode of the crystal in Hz, C_f is the sensitivity factor, n is the overtone, and Δm and Δf are the mass change and frequency change, respectively. During oxidation (deprotonation), the frequency change is reversed for a mass gain. This indicates solvent movement is dominating the mass change as it is reversibly inserted into the lattice in a movement opposite to that of proton.[42,56] Since the mass of a proton is much smaller than that of the solvent molecules assisting with hydrogen bonding, the slopes are the opposite of what is expected.[56] This was also observed when measuring NiHCF in acidic aqueous solution (Figure S18). In contrast, when measuring the frequency and mass change of NiHCF with sodium ions as the intercalating

ion in methanol, the expected mass change trend is observed (Figure 4c, blue trace). This is because sodium ions rely on ionic attraction for movement during (de)intercalation and not a hydrogen bonding network like protons.

The attraction of sodium ions to cyanide groups present in PBA dictates ion movement and therefore less interstitial water rearrangement is expected.[54] In summary, the slope of the mass change curves measured in acidic methanol solution (Figure 4c, red trace) indicates that lattice water and solvent molecule rearrangement plays a large role in the ion intercalation process, rather than being dependent on cation-anion attraction as alkali metal ions would be (Figure 4c, blue trace). [54] This is indicative of proton movement into and out of the NiHCF RR material. This proton (deintercalation) is reversible, indicated by the electrode having the same mass when fully oxidized and reduced over multiple cycles (Figure 4c, red trace). Additionally, no mass change was observed when a bare crystal was measured in the same potential range in the same solution (Figure S19) indicating the mass changes were due to the behavior of the NiHCF thin film.

Proton balanced ModES production of 4-tert-butyl benzyl acetal/aldehyde and H_2O_2

The full cycle of ModES involves two half-reactions conducted sequentially in different electrolytes with the RR switched between the two undivided cells (Figure 5a) with a three-electrode configuration. Before ModES cycling, the RR electrode (Figure S20) is fully oxidized in aqueous solution. For the methylarene oxidation reaction step, the RR electrode is washed in water and then methanol multiple times, then dried (Figure 5a). A current density of 22 mA/cm^2 is applied to the graphite rod working electrode while the RR is reduced to 25% SOC based on its capacity in aqueous solution (34 C) in the optimized supporting electrolyte of 0.1 M $TBAClO_4$ and 20 mM $NiNO_3$ in a methanol/water mixture (20:1; cf. Figure 3b). The average potential on the graphite rod is approximately 2.1 V vs. Fc/Fc^+. For the aqueous hydrogen peroxide production step at pH = 11, the applied potential was set at 0.244 V vs. RHE and the RR is oxidized back to 100% SOC with an average current density of 39 mA/cm^2. The same amount of charge was passed for the aqueous and non-aqueous half-reactions.

After 23 cycles of continuous ModES operation, full conversion of 1 mmol 4-*tert*-butyltoluene was achieved, producing the aldehyde/acetal products in 52% yield (Figure 5b and 5c, Figure S21). This corresponds to a Faradaic efficiency of 26%, which is similar to the Faradaic efficiency in the control experiment (34%; entry 8, Figure 3b). Methylarene oxidation occurs progressively within the same 10 mL cell throughout the ModES process. Modest solvent loss over time due to the repeated transfer of the RR electrode between the two reaction cells likely contributes to the yield reduction relative to the single-batch result in Figure 3b. On the cathodic side, a fresh 30 mL aqueous Na_2SO_4 solution (1.7 M, adjusted to pH = 11) under continuous bubbling of oxygen gas was used for each ModES cycle at a constant potential, producing an average of 186 ppm H_2O_2 (5.47 mM) with a FE of 93.2% (Figure 5e). Such accumulated concentration of H_2O_2 is already useful for many applications, such as disinfection and water treatment.[32] There was only a 0.4–0.7 pH unit increase per cycle during the cathodic reaction (Figure 5d). Approximately 10% of protons released during the oxidative reaction are not intercalated into the RR. Due to

the sensitivity of the methylarene oxidation reaction to excess protons, a small amount of base N,N-diisopropylethylamine (20 μL), was added every 4 cycles to the organic reaction mixture to neutralize the excess protons. XRD confirmed that the phase and crystallinity of the NiHCF RR did not change after 23 cycles of ModES, ending in the fully oxidized state (Figure S22).

Extension to another oxidation reaction (arene C–H amination) and organic solvent (acetonitrile)

With the understanding that the NiHCF redox reservoir can be used to balance electrons and protons across half reactions in different solvents, we pursued pairing another oxidation reaction with a different set of reaction conditions (Figure 6a). Yoshida *et al.* have reported an arene C–H amination reaction involving oxidative coupling of arenes with pyridine to afford arylpyrdinium products, which are then directly converted to the corresponding anilines upon treatment with piperidine.[57] The reported reactions are performed in acetonitrile using a divided cell configuration. We first conducted the Yoshida amination reaction under the reported conditions with a Pt counter cathode in divided and undivided cells to assess the influence of the cell configuration (see experimental details in the Supporting Information). These reactions afforded 72% and 6% yields of the 1-naphthylamine product, respectively (Figure S23 and S24). The low yield in the undivided cell is attributed to the facile *in situ* reduction of the arylpyridinium product at the Pt cathode.

We then repeated the reaction in an undivided cell in which the Pt cathode was replaced with the NiHCF RR as a counter electrode (Figure 6a left side). Under otherwise identical conditions, the reaction affords 1-naphthylamine in yields up to 67% (Figure 6b, S25, see full screening details in Table S2). It was necessary to include some cations in the acetonitrile solution to facilitate the ion transport and support effective cycling of the RR. Due to the sensitivity of this reaction to water, unlike the methylarene oxidation reaction described above, water could not be used as a source of H^+ cations. Addition of 100 mM acetic acid to the reaction mixture led to a 52% yield of product (Figure 6b, Figure S26). Speculating that acetic acid could hydrogen bond with pyridine in solution and limit its effectiveness as a nucleophile, we tested sodium cations for improving the reaction. The optimal yield (66%) was obtained from a reaction mixture initiated with 16 mM $NaClO_4$. The cell potential evolution during the discharge process (Figure 6b blue RR Na trace) suggests that sodium ions are readily intercalated into the RR at the early stages of the reaction, after which protons accumulated from oxidation of naphthalene undergo intercalation into the RR. This anodic arene C–H amination can proceed in an undivided cell together with the reduction of the RR electrode because the pyridinium intermediate does not decompose on the RR electrode. This is supported by CVs on platinum that show an onset potential of reduction at −0.95 V vs Fc/Fc^+ in the presence of pyridinium (Figure S27). Figure 6b shows the RR electrode remains at a potential above −0.95 V for the majority of the electrolysis. In contrast, the reduction of pyridinium has a similar potential to that seen for hydrogen evolution (Figures S27–S29).

Furthermore, use of the RR to support the electrosynthesis of H_2O_2 in aqueous solution (Figure 6a right half), following the oxidative amination of naphthalene in acetonitrile, was successful and proceeded with a Faradaic efficiency of 85%. This completes the ModES cycle and demonstrates the pairing of aqueous H_2O_2 production with another anodic organic electrosynthesis in another solvent beyond methanol, which was used in the methylarene oxidation reaction discussed above. These results suggest the potential utility of the ModES strategy for general organic electrosyntheses and also highlight the advantage that the use of RR can translate an electrolysis reaction that requires a divided cell under conventional conditions into a reaction that proceeds effectively in an undivided cell.

Conclusion

In conclusion, we demonstrate the pairing of two electrosynthetic reactions across different solvents: methylarene oxidation in methanol or naphthalene C–H amination in acetonitrile with hydrogen peroxide production in water using an ion-balanced ModES strategy. These ModES processes are enabled by a proton-selective NiHCF RR material that (de)intercalates protons to maintain pH stability for the electrochemical cells, allowing for effective methylarene oxidation or arene C–H amination, and the accumulation of H_2O_2. Careful experiments ensure and confirm the selective transport of protons through NiHCF RR from the nonaqueous anodic cell to the aqueous cathodic cell. Not only would these pairings of electrochemical reactions not be possible without the RR because of the incompatible reaction media, but also the ModES process eliminates the less productive auxiliary counter electrode reactions and the need for expensive and cumbersome ion-selective membranes used in divided electrochemical cells. These pairings show the utility of ModES by enabling the synthesis of three chemicals (both inorganic and organic) with flexibility in rate, scale, and reaction conditions.

To increase the utility of ModES in general organic electrosynthesis, the development of RR materials that have high stability, solvent compatibility, selectivity for ion transport, and high capacity is crucial. Higher capacity materials improve the practicality of ModES because many organic electrochemical reactions require large amounts of charge. The emerging proton battery materials[36,58] would be suitable candidates, but they are commonly reported in aqueous systems, so their solvent compatibility, stability, and ion selectivity need to be screened and further improved. Flexible pairing of electrochemical syntheses of products that have incompatible reaction conditions, different and variable market demand but similar local applications without sacrificial half-reactions and expensive membranes could enhance the economic viability of distributed electrochemical production.

Supplementary Material

Refer to Web version on PubMed Central for supplementary material.

Acknowledgements

This work was supported by the University of Wisconsin-Madison UW2020 grant provided by the Wisconsin Alumni Research Foundation (WARF). Z.-M.S and S.S.S. were also supported by the NIH (R35 GM134929). Spectroscopic instrumentation was partially supported by the NIH (S10 OD020022) and the NSF (CHE-1048642).

The authors gratefully acknowledge use of facilities and instrumentation supported by NSF through the University of Wisconsin-Madison Materials Research Science and Engineering Center (DMR-1720415).

References

1). Luna PD; Hahn C; Higgins D; Jaffer SA; Jaramillo TF; Sargent EH What Would It Take for Renewably Powered Electrosynthesis to Displace Petrochemical Processes? Science 2019, 364 (6438). 10.1126/science.aav3506.

(2). Wiebe A; Gieshoff T; Möhle S; Rodrigo E; Zirbes M; Waldvogel SR Electrifying Organic Synthesis. Angew. Chem., Int. Ed. 2018, 57 (20), 5594–5619. 10.1002/anie.201711060.

(3). Minteer SD; Baran P Electrifying Synthesis: Recent Advances in the Methods, Materials, and Techniques for Organic Electrosynthesis. Acc. Chem. Res. 2020, 53 (3), 545–546. 10.1021/acs.accounts.0c00049. [PubMed: 32178522]

(4). Yuan Y; Lei A Is Electrosynthesis Always Green and Advantageous Compared to Traditional Methods? Nat. Commun. 2020, 11 (1), 802. 10.1038/s41467-020-14322-z. [PubMed: 32029716]

(5). Botte GG Electrochemical Manufacturing in the Chemical Industry. Interface Mag. 2014, 23 (3), 49–55. 10.1149/2.f04143if.

(6). Novaes LFT; Liu J; Shen Y; Lu L; Meinhardt JM; Lin S Electrocatalysis as an Enabling Technology for Organic Synthesis. Chem. Soc. Rev. 2021, 50 (14), 7941–8002. 10.1039/d1cs00223f. [PubMed: 34060564]

(7). Zhong X; Hoque MA; Graaf MD; Harper KC; Wang F; Genders JD; Stahl SS Scalable Flow Electrochemical Alcohol Oxidation: Maintaining High Stereochemical Fidelity in the Synthesis of Levetiracetam. Org. Process Res. Dev. 2021. 25(12), 2601–2607.10.1021/acs.oprd.1c00036.. [PubMed: 35177894]

(8). Danly DE Development and Commercialization of the Monsanto Electrochemical Adiponitrile Process. J. Electrochem. Soc. 1984, 131 (10), 435C–442C. 10.1149/1.2115324.

(9). Hilt G Basic Strategies and Types of Applications in Organic Electrochemistry. Chemelectrochem 2020, 7 (2), 395–405. 10.1002/celc.201901799.

(10). Ibanez JG; Frontana-Uribe BA; Vasquez-Medrano R Paired Electrochemical Processes: Overview, Systematization, Selection Criteria, Design Strategies, and Projection. J. Mex. Chem. Soc. 2017, 60 (4), 247–260. 10.29356/jmcs.v60i4.117.

(11). Sbei N; Hardwick T; Ahmed N Green Chemistry: Electrochemical Organic Transformations via Paired Electrolysis. ACS Sustainable Chem. Eng. 2021, 9 (18), 6148–6169. 10.1021/acssuschemeng.1c00665.

(12). Martínez NP; Isaacs M; Nanda KK Paired Electrolysis for Simultaneous Generation of Synthetic Fuels and Chemicals. New J. Chem. 2020, 44 (15), 5617–5637. 10.1039/c9nj06133a.

(13). Aust N; Kirste A Encyclopedia of Applied Electrochemistry. 2014, 1505–1510. 10.1007/978-1-4419-6996-5_370.

(14). Frontana-Uribe BA; Little RD; Ibanez JG; Palma A; Vasquez-Medrano R Organic Electrosynthesis: A Promising Green Methodology in Organic Chemistry. Green Chem. 2010, 12 (12), 2099–2119. 10.1039/c0gc00382d.

(15). Sheng H; Janes AN; Ross RD; Hofstetter H; Lee K; Schmidt JR; Jin S Linear Paired Electrochemical Valorization of Glycerol Enabled by the Electro-Fenton Process Using a Stable NiSe2 Cathode. Nat. Catal. 2022, 5 (8), 716–725. 10.1038/s41929-022-00826-y.

(16). Llorente MJ; Nguyen BH; Kubiak CP; Moeller KD Paired Electrolysis in the Simultaneous Production of Synthetic Intermediates and Substrates. J. Am. Chem. Soc. 2016, 138 (46), 15110–15113. 10.1021/jacs.6b08667. [PubMed: 27933880]

(17). Hermann P; Heinz H Preparation of Phthalides. US6063256A, May 16, 2000.

(18). Stecker F; Fischer A; Botzem J; Griesbach U; Pelzer R Electrochemical Method for Producing 3-Tert-Butylbenzaldehyde Dimethyl Acetal. US8629304B2, January 14, 2014.

(19). Wu T; Moeller KD Organic Electrochemistry: Expanding the Scope of Paired Reactions. Angew. Chem., Int. Ed. 2021, 60 (23), 12883–12890. 10.1002/anie.202100193.

(20). Wang F; Li W; Wang R; Guo T; Sheng H; Fu H-C; Stahl SS; Jin S Modular Electrochemical Synthesis Using a Redox Reservoir Paired with Independent Half-Reactions. Joule 2021, 5 (1), 149–165. 10.1016/j.joule.2020.11.011.

(21). Wallace AG; Symes MD Decoupling Strategies in Electrochemical Water Splitting and Beyond. Joule 2018, 2 (Nat. Chem. 5 2013), 1390–1395. 10.1016/j.joule.2018.06.011.

(22). Dotan H; Landman A; Sheehan SW; Malviya KD; Shter GE; Grave DA; Arzi Z; Yehudai N; Halabi M; Gal N; Hadari N; Cohen C; Rothschild A; Grader GS Decoupled Hydrogen and Oxygen Evolution by a Two-Step Electrochemical–Chemical Cycle for Efficient Overall Water Splitting. Nat. Energy 2019, 4 (9), 786–795. 10.1038/s41560-019-0462-7.

(23). Chen L; Dong X; Wang Y; Xia Y Separating Hydrogen and Oxygen Evolution in Alkaline Water Electrolysis Using Nickel Hydroxide. Nat. Commun. 2016, 7 (1), 11741. 10.1038/ncomms11741. [PubMed: 27199009]

(24). Wang F; Sheng H; Li W; Gerken JB; Jin S; Stahl SS Stable Tetrasubstituted Quinone Redox Reservoir for Enhancing Decoupled Hydrogen and Oxygen Evolution. ACS Energy Lett. 2021, 6 (4), 1533–1539. 10.1021/acsenergylett.1c00236. [PubMed: 34017916]

(25). Rausch B; Symes MD; Chisholm G; Cronin L Decoupled Catalytic Hydrogen Evolution from a Molecular Metal Oxide Redox Mediator in Water Splitting. Science 2014, 345 (6202), 1326–1330. 10.1126/science.1257443. [PubMed: 25214625]

(26). Landman A; Dotan H; Shter GE; Wullenkord M; Houaijia A; Maljusch A; Grader GS; Rothschild A Photoelectrochemical Water Splitting in Separate Oxygen and Hydrogen Cells. Nat. Mater. 2017, 16 (6), 646–651. 10.1038/nmat4876. [PubMed: 28272504]

(27). Symes MD; Cronin L Decoupling Hydrogen and Oxygen Evolution during Electrolytic Water Splitting Using an Electron-Coupled-Proton Buffer. Nat. Chem. 2013, 5 (5), 403–409. 10.1038/nchem.1621. [PubMed: 23609091]

(28). Wang R; Sheng H; Wang F; Li W; Roberts DS; Jin S Sustainable Coproduction of Two Disinfectants via Hydroxide-Balanced Modular Electrochemical Synthesis Using a Redox Reservoir. ACS Cent. Sci. 2021, 7 (12), 2083–2091. 10.1021/acscentsci.1c01157. [PubMed: 34963900]

(29). Vantourout JC From Bench to Plant: An Opportunity for Transition Metal Paired Electrocatalysis. Org. Process Res. Dev. 2021, 25 (12), 2581–2586. 10.1021/acs.oprd.1c00046.

(30). Perry SC; Pangotra D; Vieira L; Csepei L-I; Sieber V; Wang L; León C. P.de; Walsh FC Electrochemical Synthesis of Hydrogen Peroxide from Water and Oxygen. Nat. Rev. Chem. 2019, 3 (7), 442–458. 10.1038/s41570-019-0110-6.

(31). Murray AT; Voskian S; Schreier M; Hatton TA; Surendranath Y Electrosynthesis of Hydrogen Peroxide by Phase-Transfer Catalysis. Joule 2019, 3(12), 2942–2954. 10.1016/j.joule.2019.09.019.

(32). Yang S; Verdaguer-Casadevall A; Arnarson L; Silvioli L; Čolić V; Frydendal R; Rossmeisl J; Chorkendorff I; Stephens IEL Toward the Decentralized Electrochemical Production of H2O2: A Focus on the Catalysis. ACS Catal. 2018, 8 (5), 4064–4081. 10.1021/acscatal.8b00217.

(33). Wang R; Sheng H; Wang F; Li W; Roberts DS; Jin S Sustainable Coproduction of Two Disinfectants via Hydroxide-Balanced Modular Electrochemical Synthesis Using a Redox Reservoir. ACS Cent. Sci. 2021, 7 (12), 2083–2091. 10.1021/acscentsci.1c01157. [PubMed: 34963900]

(34). Zeng JS; Manthiram K Redox Reservoirs: Enabling More Modular Electrochemical Synthesis. Trends Chem. 2020, 3 (3), 157–159. 10.1016/j.trechm.2020.12.010.

(35). Wu X; Hong JJ; Shin W; Ma L; Liu T; Bi X; Yuan Y; Qi Y; Surta TW; Huang W; Neuefeind J; Wu T; Greaney PA; Lu J; Ji X Diffusion-Free Grotthuss Topochemistry for High-Rate and Long-Life Proton Batteries. Nat. Energy 2019, 4 (2), 123–130. 10.1038/s41560-018-0309-7.

(36). Xu Y; Wu X; Ji X The Renaissance of Proton Batteries. Small Struct. 2021, 2000113. 10.1002/sstr.202000113.

(37). Yi H; Qin R; Ding S; Wang Y; Li S; Zhao Q; Pan F Structure and Properties of Prussian Blue Analogues in Energy Storage and Conversion Applications. Adv. Funct. Mater. 2021, 31 (6), 2006970. 10.1002/adfm.202006970.

(38). Simonov A; Baerdemaeker TD; Boström HLB; Gómez MLR; Gray HJ; Chernyshov D; Bosak A; Bürgi H-B; Goodwin AL Hidden Diversity of Vacancy Networks in Prussian Blue Analogues. Nature 2020, 578 (7794), 256–260. 10.1038/s41586-020-1980-y. [PubMed: 32051599]

(39). Wu X; Sun M; Guo S; Qian J; Liu Y; Cao Y; Ai X; Yang H Vacancy-Free Prussian Blue Nanocrystals with High Capacity and Superior Cyclability for Aqueous Sodium-Ion Batteries. Chemnanomat 2015, 1 (3), 188–193. 10.1002/cnma.201500021.

(40). Lumley MA; Nam D-H; Choi K-S Elucidating Structure–Composition–Property Relationships of Ni-Based Prussian Blue Analogues for Electrochemical Seawater Desalination. ACS Appl. Mater. Interfaces 2020, 12 (32), 36014–36025. 10.1021/acsami.0c08084. [PubMed: 32805788]

(41). Wu X; Qiu S; Xu Y; Ma L; Bi X; Yuan Y; Wu T; Shahbazian-Yassar R; Lu J; Ji X Hydrous Nickel–Iron Turnbull's Blue as a High-Rate and Low-Temperature Proton Electrode. ACS Appl. Mater. Interfaces 2020, 12 (8), 9201–9208. 10.1021/acsami.9b20320. [PubMed: 32011119]

(42). Komayko AI; Ryazantsev SV; Trussov IA; Arkharova NA; Presnov DE; Levin EE; Nikitina VA The Misconception of Mg2+ Insertion into Prussian Blue Analogue Structures from Aqueous Solution. Chemsuschem 2021, 14 (6), 1574–1585. 10.1002/cssc.202002916. [PubMed: 33512766]

(43). Shi L; Newcomer E; Son M; Pothanamkandathil V; Gorski CA; Galal A; Logan BE Metal-Ion Depletion Impacts the Stability and Performance of Battery Electrode Deionization over Multiple Cycles. Environ. Sci. Technol. 2021, 55 (8), 5412–5421. 10.1021/acs.est.0c08629. [PubMed: 33784453]

(44). Silva J. A. B. da; Moreira FGB; Santos V. M. L. dos; Longo RL Hydrogen Bond Networks in Water and Methanol with Varying Interaction Strengths. Phys. Chem. Chem. Phys. 2010, 13 (2), 593–603. 10.1039/c0cp01204a. [PubMed: 21042611]

(45). Merk C; Huber G Process for Electrochemical Oxidation of Organic Compounds. US6398938B2, June 4, 2002.

(46). Zhang X; Xia Y; Xia C; Wang H Insights into Practical-Scale Electrochemical H2O2 Synthesis. Trends Chem. 2020, 2 (10), 942–953. 10.1016/j.trechm.2020.07.007.

(47). Lu Z; Chen G; Siahrostami S; Chen Z; Liu K; Xie J; Liao L; Wu T; Lin D; Liu Y; Jaramillo TF; Nørskov JK; Cui Y High-Efficiency Oxygen Reduction to Hydrogen Peroxide Catalysed by Oxidized Carbon Materials. Nat. Catal. 2018, 1 (2), 156–162. 10.1038/s41929-017-0017-x.

(48). Jiang K; Back S; Akey AJ; Xia C; Hu Y; Liang W; Schaak D; Stavitski E; Nørskov JK; Siahrostami S; Wang H Highly Selective Oxygen Reduction to Hydrogen Peroxide on Transition Metal Single Atom Coordination. Nat. Commun. 2019, 10 (1), 3997. 10.1038/s41467-019-11992-2. [PubMed: 31488826]

(49). Agmon N The Grotthuss Mechanism. Chem. Phys. Lett. 1995, 244 (5–6), 456–462. 10.1016/0009-2614(95)00905-j.

(50). Poli I; Eslava S; Cameron P Tetrabutylammonium Cations for Moisture-Resistant and Semitransparent Perovskite Solar Cells. J. Mater. Chem. A 2017, 5 (42), 22325–22333. 10.1039/c7ta06735f.

(51). Ojwang DO; Grins J; Wardecki D; Valvo M; Renman V; Häggström L; Ericsson T; Gustafsson T; Mahmoud A; Hermann RP; Svensson G Structure Characterization and Properties of K-Containing Copper Hexacyanoferrate. Inorg Chem. 2016, 55 (12), 5924–5934. 10.1021/acs.inorgchem.6b00227. [PubMed: 27258790]

(52). Israelachvili JN Intermolecular and Surface Forces (Third Edition). Part Forces Atoms Mol. 2011, 71–90. 10.1016/b978-0-12-375182-9.10004-1.

(53). Lam RK; Smith JW; Saykally RJ Communication: Hydrogen Bonding Interactions in Water-Alcohol Mixtures from X-Ray Absorption Spectroscopy. J. Chem. Phys. 2016, 144 (19), 191103. 10.1063/1.4951010. [PubMed: 27208929]

(54). Nordstrand J; Toledo-Carrillo E; Vafakhah S; Guo L; Yang HY; Kloo L; Dutta J Ladder Mechanisms of Ion Transport in Prussian Blue Analogues. ACS Appl. Mater. Interfaces 2022, 14 (1), 1102–1113. 10.1021/acsami.1c20910. [PubMed: 34936348]

(55). Sauerbrey G Verwendung von Schwingquarzen Zur Wägung Dünner Schichten Und Zur Mikrowägung. Zeitschrift Für Physik 1959, 155 (2), 206–222. 10.1007/bf01337937.

(56). Jiang H; Hong JJ; Wu X; Surta TW; Qi Y; Dong S; Li Z; Leonard DP; Holoubek JJ; Wong JC; Razink JJ; Zhang X; Ji X Insights on the Proton Insertion Mechanism in the Electrode of Hexagonal Tungsten Oxide Hydrate. J. Am. Chem. Soc. 2018, 140 (37), 11556–11559. 10.1021/jacs.8b03959. [PubMed: 30180554]

(57). Morofuji T; Shimizu A; Yoshida J Electrochemical C–H Amination: Synthesis of Aromatic Primary Amines via N-Arylpyridinium Ions. J. Am. Chem. Soc. 2013, 135 (13), 5000–5003. 10.1021/ja402083e. [PubMed: 23510504]

(58). Liang G; Mo F; Ji X; Zhi C Non-Metallic Charge Carriers for Aqueous Batteries. Nat. Rev. Mater. 2021, 6 (2), 109–123. 10.1038/s41578-020-00241-4.

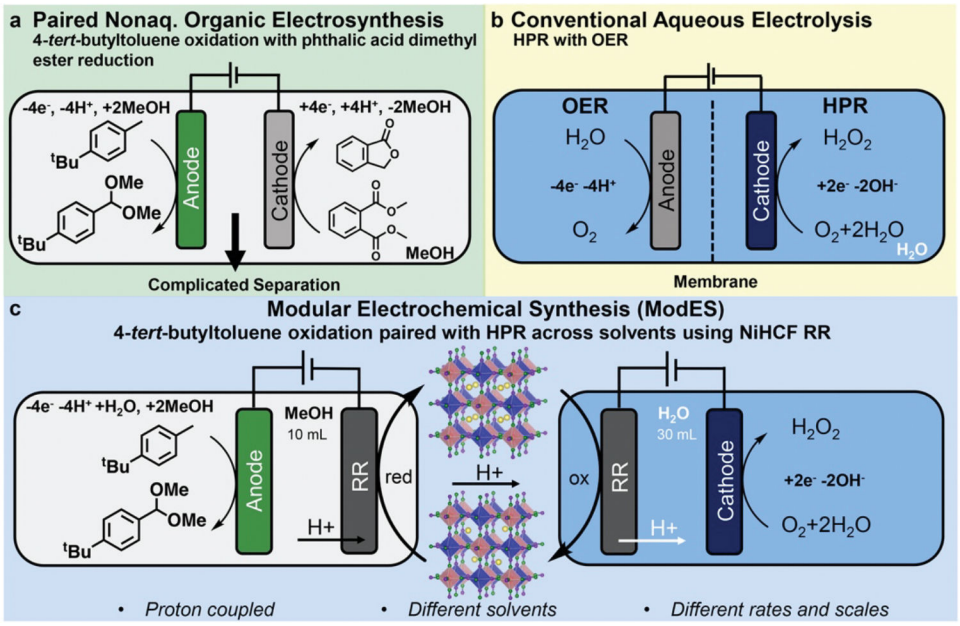

Figure 1. Schematic illustration of RR enabled ModES for paired oxidation of 4-*tert*-butyltoluene in methanol and reduction of oxygen to H_2O_2 in water in comparison to conventional electrolysis processes.

(a) Schematic of the BASF paired electrolysis that takes place in methanol where two organic products are synthesized simultaneously at both the cathode and anode. (b) In conventional electrochemical H_2O_2 production, the non-productive OER takes place on the anode to charge balance the cathodic reaction. This process requires a membrane to prevent H_2O_2 decomposition on the anode. (c) In the ModES process, the anodic and cathodic processes take place in two undivided cells and a RR electrode serves as the counter electrode for the process of interest, storing ions and charge, and ensuring ion balance. This allows the two reactions to take place in different solvents, with different scales, rates, and without a complicated separation process.

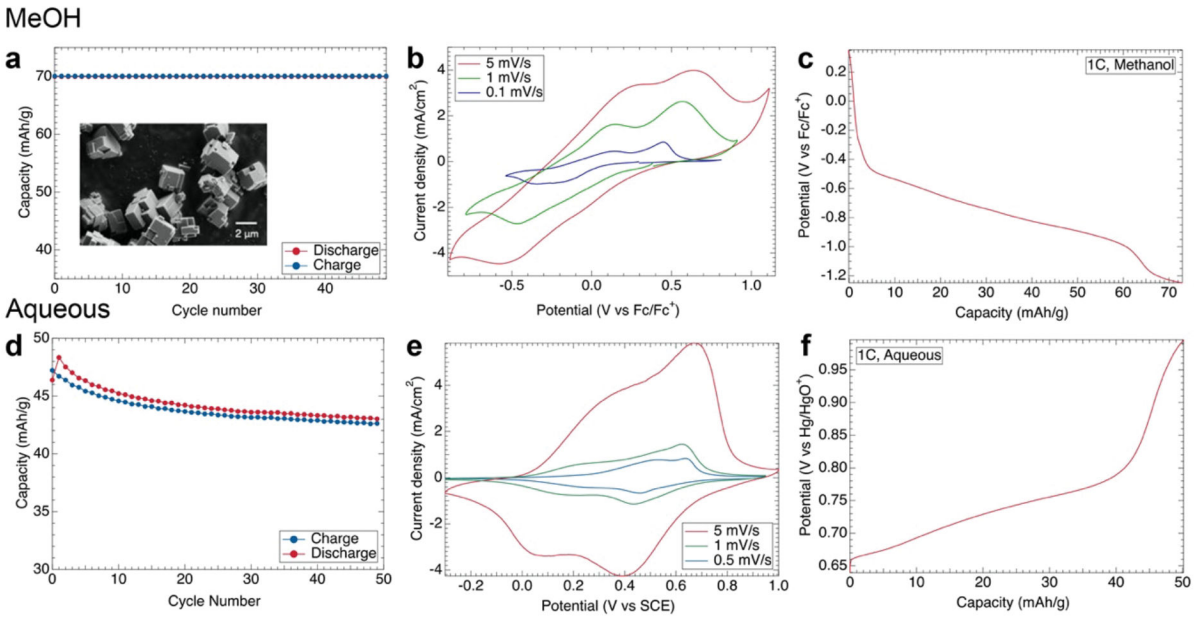

Figure 2. Electrochemical characterizations of the NiHCF RR material in both aqueous and methanol solutions.

(a) Galvanostatic charge-discharge tests in a methanol solution containing 0.1 M $TBAClO_4$, 20 mM $NiNO_3$, and 0.01 M H_2SO_4 with a NiHCF working electrode (WE) and counter electrode (CE). Inset shows a representative SEM image of NiHCF crystals. (b) Cyclic voltammograms of NiHCF in 0.1 M $TBAClO_4$ and 0.01 M H_2SO_4 in methanol at a scan rate from 0.1 to 5 mV/s. (c) Galvanostatic discharge curve of NiHCF in methanol with 0.1 M $TBAClO_4$, 20 mM $NiNO_3$, and 0.01 M H_2SO_4. (d) Galvanostatic charge-discharge tests in aqueous 0.5 M H_2SO_4 with a NiHCF WE and CE. (e) CVs of NiHCF conducted in 0.5 M H_2SO_4 at a scan rate of 0.5, 1, and 5 mV/s. (f) Galvanostatic charge curve of NiHCF in 1.7 M Na_2SO_4 and 1 mM NaOH (pH 11) after discharge in MeOH.

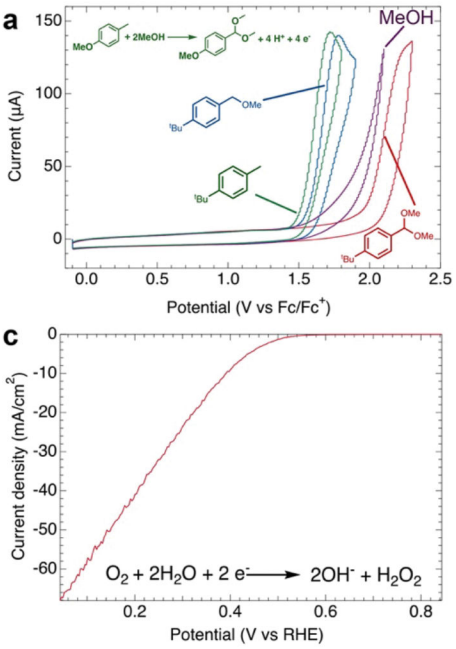

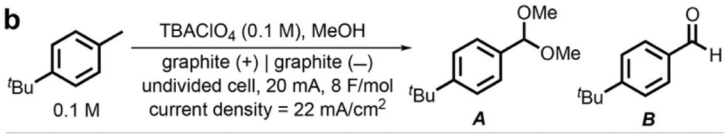

Entry	Deviation from above	Avg. cell potential (V)	A (%)	B (%)	Yield[a] (A+B, %)
1	None	5.0	68	0	68 (67)
2[b]	4 F/mol	5.1	40	0	40
3	10 F/mol	5.0	56	0	56
4	current density = 15 mA/cm^2	5.0	55	0	55
5	current density = 30 mA/cm^2	5.4	52	0	52
6	$TBAPF_6$ intead of $TBACIO_4$	5.2	57	0	57
7	$MeOH/H_2O$ (20/1)	4.7	35	29	64
8	**$MeOH/H_2O$ (20/1), added 20 mM $Ni(NO_3)_2{\cdot}6H_2O$**	**4.8**	**36**	**29**	**65 (63)[c]**
9	Added 10 mM HCl	5.0	55	3	58
10	Added 50 mM HCl	4.1	30	0	30

See Supporting Information for experimental details. [a] Yield determined by ^{1}H NMR analysis of the crude reaction mixture using mesitylene as an internal standard, yields shown in parentheses are isolated. [b] Recovered 36% starting material. [c] Hydrolysis was performed to convert acetals to aldehydes before isolation, the yield corresponds to isolated aldehydes.

Figure 3. Electrochemical behaviors and product distributions of the separate electrochemical half-reactions.

(a) CV data relevant to methylarene oxidation. Conditions: 0.1 M $TBAPF_6$ in acetonitrile, glassy carbon working electrode, Pt wire counter electrode, reference electrode $Ag/AgNO_3$ (10 mM $AgNO_3$ in acetonitrile) corrected vs. Fc/Fc^+. Oxidation of methanol prevents overoxidation of the acetal and aldehyde to the carboxylic acid. (b) Table for optimizing the product yield and distributions of methylarene oxidation with graphite rod working and counter electrode. Entries 1–6 show optimization of the half reaction. Entries 7–8 reflect conditions used to improve the anticipated performance of the RR. Entries 9–10 show the sensitivity of the reaction to excess proton concentration. (c) Linear scanning voltammetry curve (LSV) for the cathodic production of H_2O_2 using an Fe-CNT electrode with an area of 2 cm^2 at a scan rate of 10 mV/s in O_2 saturated 1.7 M Na_2SO_4 (adjusted to pH = 11) with a Pt counter electrode.

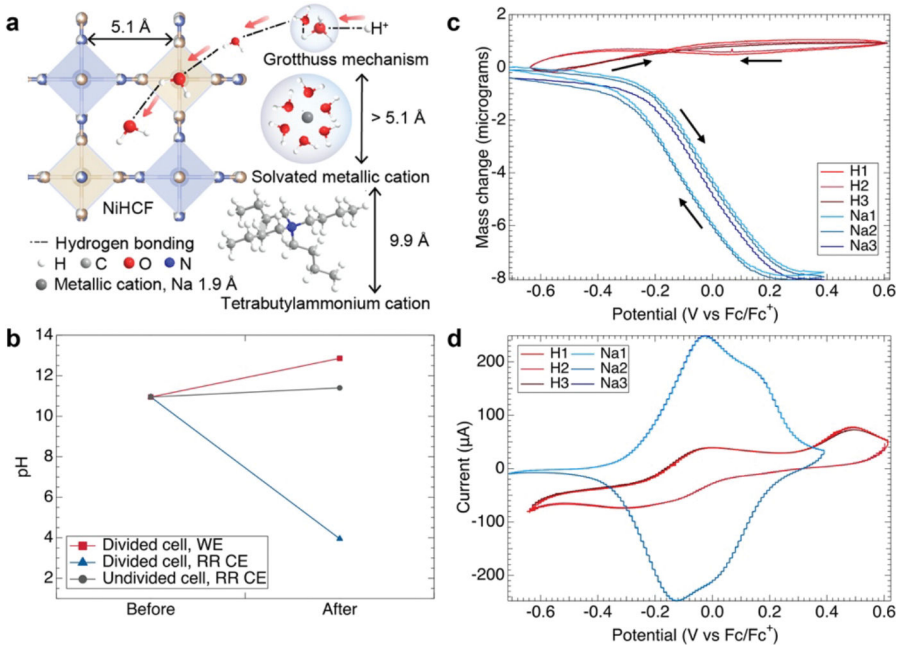

Figure 4. Proton-balancing ability of the NiHCF RR

(a) Schematic of the Grotthuss mechanism, size of ions, and NiHCF cage illustrating the role of hydrogen bonding and the need to minimize ion competition. (b) pH shifts showing proton intercalation and deintercalation ability of the RR. A pH 11 solution was used in both the undivided and divided cell. The RR was reduced in 1 M H_2SO_4 in methanol and then oxidized, releasing protons in the respective cells. H_2O_2 production was performed at the working electrode to ensure proton release. (c) Electrochemical quartz crystal microbalance measured mass change of proton (de)intercalation of NiHCF in 1:20 water:methanol solution of 1 mM H_2SO_4, 20 mM $NiNO_3$, 0.1 M $TBAClO_4$ in comparison with sodium (de)intercalation in 0.1 M Na_2SO_4 in methanol. Slope trends are opposite of each other due to their differing (de)intercalation mechanisms. (d) The corresponding CVs during the measurements of the mass changes in (c).

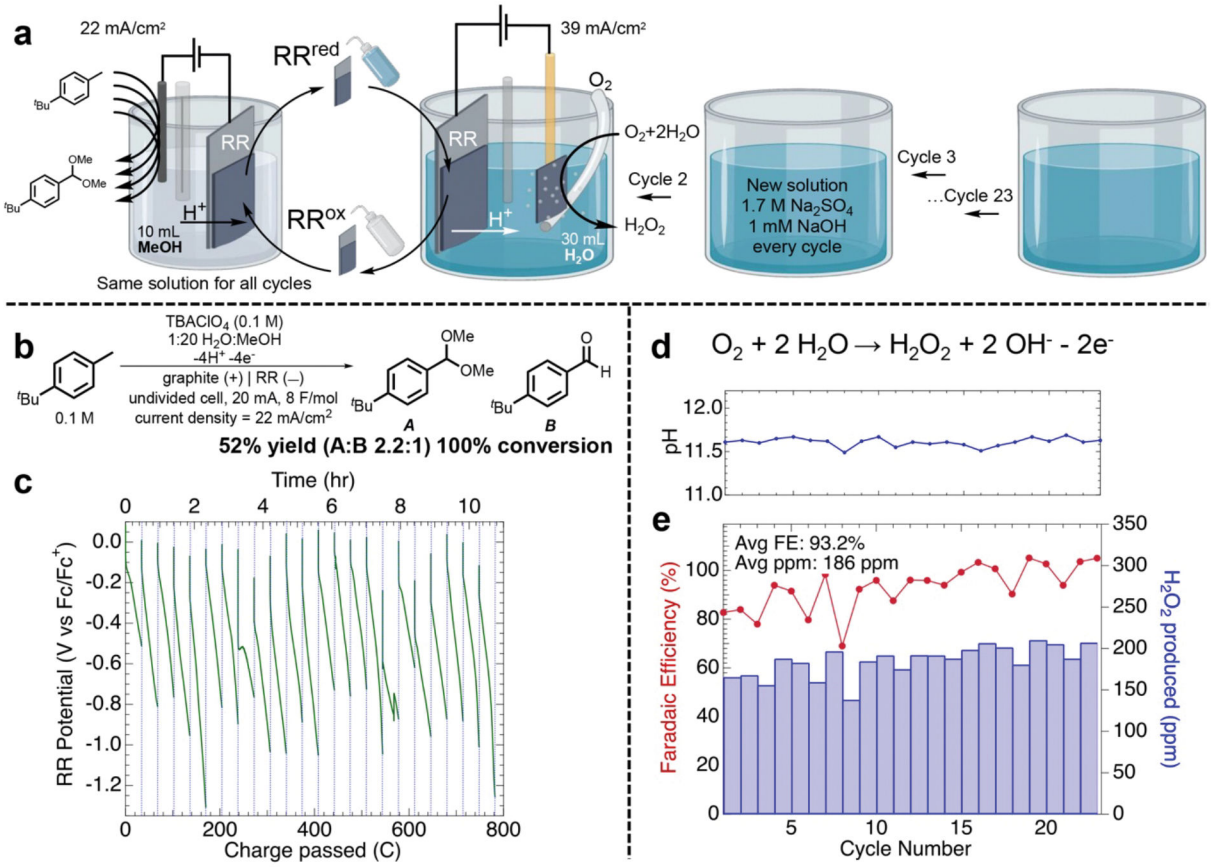

Figure 5. Modular electrosynthesis of 4-tert-butylbenzylaldehyde in methanol and H_2O_2 in aqueous solution enabled by the proton selective NiHCF RR.

(a) Full schematic of the ModES process for pairing methylarene oxidation reaction and H_2O_2 production. (b) Reaction schematic of methylarene oxidation to 4-tert-butylbenzaldehyde and acetal product resulting from 23 cycles of ModES with the product yields. (c) Potential of the NiHCF RR paired with methylarene oxidation over 23 ModES cycles. (d) Reaction equation and pH after H_2O_2 production for each cycle. The electrolyte had a starting pH of 11 and shifted minimally during the production of 200 ppm H_2O_2 showing pH stability over the course of the ModES cycling. (e) Faradaic efficiency and concentration of H_2O_2 produced in the aqueous cell for each ModES cycle. A new 30 mL solution was used each cycle.

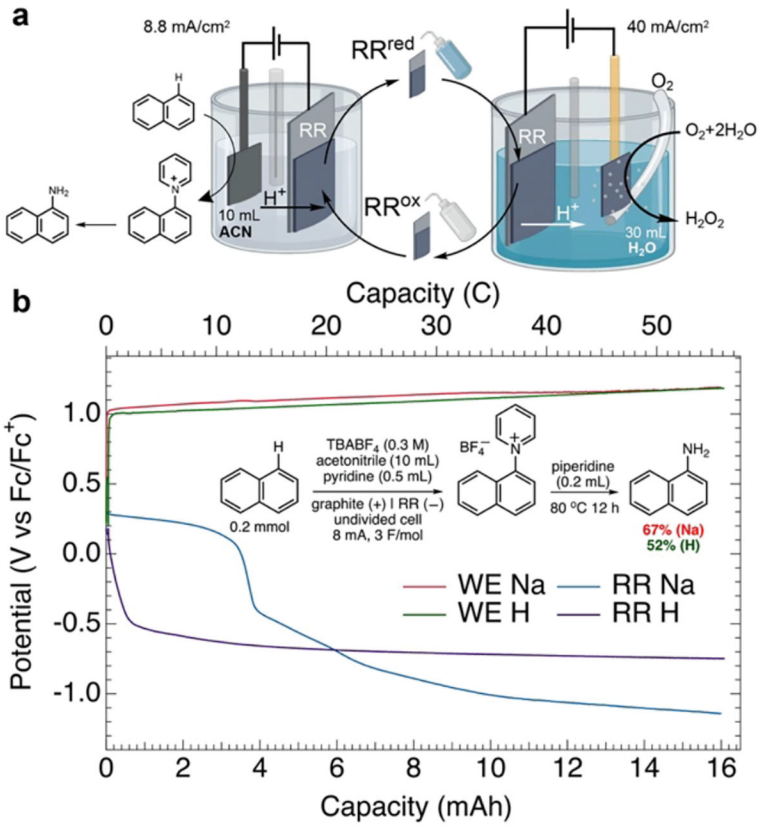

Figure 6. Modular electrosynthesis of 1-napthylamine in acetonitrile and H_2O_2 in aqueous solution enabled by the NiHCF RR.

(a) Full schematic of the ModES process for pairing the oxidative C–H amination of naphthalene and H_2O_2 production. (b) Potential evolution of the NiHCF RR counter electrode and carbon felt working electrode during naphthalene amination with $NaClO_4$ (blue and red traces, respectively) and acetic acid (purple and green traces, respectively) added in the electrolyte. Inset shows the reaction schematic for naphthalene amination and the resulting product yields.